14th World Congress on Computational Mechanics (WCCM)
ECCOMAS Congress 2020)
19–24 July 2020, Paris, France
F. Chinesta, R. Abgrall, O. Allix and M. Kaliske (Eds)

NUMERICAL MODELING OF TWO-PHASE FLOW WITH CONTACT DISCONTINUITIES

RONALD A. REMMERSWAAL* AND ARTHUR E.P. VELDMAN†

Johann Bernoulli Institute, University of Groningen
Nijenborgh 9, 9747 AG Groningen, The Netherlands
* r.a.remmerswaal@rug.nl † a.e.p.veldman@rug.nl

Key words: two-phase flow, contact discontinuity, breaking waves

Abstract. When simulating high Reynolds number two-phase flow, boundary layers develop at the interface, which are much thinner compared to the capillary length-scales that are of interest. Resolving such an interface boundary layer is expensive and therefore it is often not resolved in a simulation.

Numerically such an underresolved interface boundary layer results in a velocity discontinuity tangential to the interface. We propose to include such tangential velocity discontinuities in our numerical model. This results in a sharp two-fluid model for two-phase flow, where only the interface-normal component of the velocity field is smooth. This condition is implicitly enforced via a new jump condition on the pressure gradient, which we discretize using a multidimensional variant of the ghost fluid method [5].

Results are shown of breaking waves [2] as well as (breaking) waves impacting a solid wall [3] where we compare to state-of-the-art methods [3, 4]. We show that our proposed method is able to accurately simulate high Reynolds number two-phase flow without the need for resolving, or artificially thickening, of the interface boundary layer.

1 INTRODUCTION

Numerical simulations can facilitate in the understanding of the physics underlying the obeserved variability in impact pressures during breaking wave impacts [3]. One of the mechanism deemed responsible for pressure variability is the development of free surface instabilities at the wave crest. Numerical investigation of free surface instabilities on a breaking wave crest requires resolving the capillary length scales, amongst which the Kelvin-Helmholtz length scale[1] will be most restrictive. Due to viscous effects, an interface boundary layer will form at the fluid interface, whose thickness [2] λ^{BL} is estimated to be significantly smaller than the capillary length scale that we are interested in resolving

$$\frac{\lambda^{\mathrm{BL}}}{\lambda^{\mathrm{KH}}} \approx \frac{\sqrt{|\,[\![u_\tau]\!]\,|}}{35}, \tag{1}$$

where $[\![u_\tau]\!]$ is the tangential velocity difference accross the interface. To that end we propose to model the interface boundary layer by letting the velocity field be discontinuous in the interface tangential direction. **using LNG and NG, what about water and air?**

[1] Here λ^{KH} denotes the fastest growing wavelength according to linearized potential flow theory.
[2] This length scale is estimated using the Blasius boundary layer approximation for a single phase flow.

In Section 2 we describe the continuous model which will be discretized in Section 3. Results are shown in Section 4 followed by concluding remarks in Section 5.

2 MATHEMATICAL MODEL

We consider a d-dimensional domain $\Omega \subset \mathbb{R}^d$, which is separated by a time-dependent interface $I(t)$ resulting in a liquid domain $\Omega^l(t)$ and a gaseous domain $\Omega^g(t)$. Since the Navier-Stokes equations are equal for the liquid and gas phase, we state them for the π-phase, where we consider $\pi \in \{l,g\}$.

At the interface we define the jump of some function α in the following way

$$[\![\alpha]\!](\mathbf{x}) = \alpha^g(\mathbf{x}) - \alpha^l(\mathbf{x}) = \lim_{s\to 0^+} \alpha(\mathbf{x}+s\eta) - \lim_{s\to 0^-} \alpha(\mathbf{x}+s\eta), \quad \mathbf{x} \in I, \tag{2}$$

where η denotes the interface normal pointing into the gas phase. Similarly we define the sum as

$$\{\!\{\alpha\}\!\} = \alpha^g + \alpha^l. \tag{3}$$

2.1 Two fluid model

We model the two phase flow using a two fluid model, where each of the phases is modeled by the incompressible Navier-Stokes equations, which we write here in conservative form on some arbitrary and fixed control volume $\omega \subset \Omega$

$$\frac{d}{dt}\int_{\omega^\pi} \rho^\pi \; dV + \int_{\partial\omega^\pi \setminus I} \rho^\pi u_\eta^\pi \; dS = 0 \tag{4}$$

$$\frac{d}{dt}\int_{\omega^\pi} \rho^\pi \mathbf{u}^\pi \; dV + \int_{\partial\omega^\pi \setminus I} \rho^\pi \mathbf{u}^\pi u_\eta^\pi \; dS = \int_{\partial\omega^\pi} [(-p^\pi + \rho^\pi \mathbf{g}\cdot\mathbf{x})\mathbf{I} + \mu^\pi \mathbf{S}^\pi]\cdot\eta \; dS, \tag{5}$$

where $\omega^\pi(t) = \omega \cap \Omega^\pi(t)$, and $\rho, p, \mathbf{g}, \mathbf{u}, \mathbf{S}$ denote the density, pressure, gravitational acceleration, velocity and symmetric part of the velocity gradient respectively. The Navier-Stokes equations are supplemented with appropriate boundary conditions (usually slip) and an evolution equation for the interface

$$\frac{d}{dt}\mathbf{x} = \mathbf{u}^\pi(\mathbf{x},t), \quad \forall \mathbf{x} \in I(t), \tag{6}$$

where the interface motion may thus be modeled by either of the two velocities. The following velocity jump condition then uniquely determines the interface evolution

$$[\![u_\eta]\!] = 0, \tag{7}$$

where $u_\eta = \mathbf{u}\cdot\eta$. Furthermore we impose the Young-Laplace equation on the interface to model the effect of surface tension (we ommit the jump in the diffusive stresses)

$$[\![p]\!] = -\sigma\kappa, \tag{8}$$

where the interface mean curvature is denoted by κ and σ denotes the surface energy coefficient.

We choose to combine the two mass conservation equations in the following way (making use of $|\omega| = |\omega^l| + |\omega^g|$)

$$\frac{d}{dt}\int_{\omega^l} \; dV + \int_{\partial\omega^l \setminus I} \mathbf{u}^l \cdot \eta \; dS = 0 \tag{9}$$

$$\int_{\partial\omega} \mathbf{u} \cdot \eta \; dS = 0, \tag{10}$$

where the first equation is a volumetric contraint on the evolution equation of the interface, and the second equation states that the mixture velocity field is divergence free.

2.2 Velocity discontinuities

Note that if $\mu^\pi = 0$ then the velocity field can develop tangential velocity discontinuities $[\![u_\tau]\!] \neq 0$ due to surface tension and/or gravity, where $\tau \perp \eta$ is a vector tangent to the interface. If $\mu^\pi > 0$ then the Navier-Stokes solution will be smooth $[\![u_\tau]\!] = 0$, numerically we however do not enforce this, as motivated in the introduction.

3 NUMERICAL MODEL

The numerical model is implemented in our in-house free surface Navier-Stokes solver ComFLOW which makes use of local and adaptive mesh refinement [10]. For simplicity in presentation however, we will assume the mesh to be rectilinear. The variables are arranged according to an Arakawa C-grid.

3.1 Notation

We denote the set of all cells by $\mathcal{C}$ and the set of all faces by $\mathcal{F}$, where the faces of one particular cell c are denoted by $\mathcal{F}(c) \subset \mathcal{F}$ and the cells neighbouring one particular face f are denoted by $\mathcal{C}(f) \subset \mathcal{C}$.

Functions $p : c \mapsto p_c \approx p(\mathbf{x}_c)$ live in the function space denoted by $\mathcal{C}^h$, where $\mathbf{x}_c$ is the centroid of the cell c. Similar definitions hold for $\mathcal{F}^h$, with $u : f \mapsto u_f \approx \eta_f \cdot \mathbf{u}(\mathbf{x}_f)$, where η_f is the face normal. The function $\alpha : \mathcal{C} \times \mathcal{F} \to \{-1, +1\}$ encodes the orientation of the face normal such that $\alpha_{c,f}\eta_f$ is outward pointing relative to the cell c. The staggered control volume belonging to some face f is denoted by ω_f.

3.2 Interface model

The interface is tracked using a volume of fluid (VoF) method combined with a geometric PLIC reconstruction.

3.2.1 Representation

The interface is represented using the volume fraction field $\bar{\chi}^l \in \mathcal{C}^h$, which is defined as $\bar{\chi}^\pi_c = \frac{|c^\pi|}{|c|}$. During the interface advection step the mass fluxes are computed using a geometric PLIC reconstruction of the interface: per cell c we find a normal vector η_{i_c} and plane constant s_c such that

$$c^l = \{\, \mathbf{x} \in c \mid \eta_{i_c} \cdot (\mathbf{x} - \mathbf{x}_c) \leq s_c \,\}, \quad c^g = c \setminus c^l. \tag{11}$$

Computation of the normal vector is done using either local height functions (LHFs) or the efficient least-squares VoF reconstruction algorithm (ELVIRA) [7] if insufficiently many LHFs are available. Using the interface reconstructions we then define the staggered volume fractions $\bar{\chi}^{\pi} \in \mathcal{F}^h$ and the phase domains

$$\bar{\chi}_f^{\pi} = \frac{|\omega_f^{\pi}|}{|\omega_f|}, \quad \omega_f^{\pi} = \omega \cap \Omega^{\pi}, \quad \Omega^{\pi} = \bigcup_{c \in \mathcal{C}} c^{\pi}. \tag{12}$$

The face apertures is given by $a_f^{\pi} = \frac{|f^{\pi}|}{|f|}$, where f^{π} is the part of the face f which contains the π-phase. Note that f^{π} is not uniquely defined since the PLIC reconstruction is not continuous accross the faces, therefore we average the face aperture using the two neighbouring cells $c \in \mathcal{C}(f)$.

For the modeling of surface tension we compute the interface curvature $\kappa \in \mathcal{C}^h$ using the volume fractions as per the LHF method or generalized LHF method [8] if insufficiently many LHFs are available.

3.2.2 Advection

In case of a single fluid we summarize the interface advection in the following way

$$\bar{\chi}^{l,(n+1)} = \bar{\chi}^{l,(n)} - \Delta t D m^{l,(n)} \tag{13}$$

where D is the discrete divergence operator (see Section 3.4.1) and

$$\Delta t |f| m^{l,(n)} \approx \int_{t^{(n)}}^{t^{(n+1)}} \int_{f^l} u_{\eta} \; dS \; d\tau, \tag{14}$$

is computed using the volume enforced flux polygons as per the EMFPA scheme [6]. Here the Lagrangian backtracking of the face f, resulting in the flux polygon $P_f^{(n)} = P^{\text{EMFPA}}(f, -\Delta t u^{(n)})$, is according to (6), whereas the enforcement step tries to ensure that (9) holds exactly (here we consider the volume of the flux polygon to be signed)

$$|P_f^{(n)}| = \Delta t |f| u^{(n)}. \tag{15}$$

The mass flux is then given by

$$\Delta t |f| m_f^{l,(n)} = |P_f^{(n)} \cap \Omega^{l,(n)}|. \tag{16}$$

We now modify the original EMFPA scheme (in case of a velocity discontinuity) by redefining the flux polygon as

$$P_f^{(n)} = P_f^{l,(n)} \cup P_f^{g,(n)}, \quad P_f^{\pi,(n)} = P^{\text{EMFPA}}(f^{\pi,(n)}, -\Delta t u^{\pi,(n)}), \tag{17}$$

and the volume enforcement step is replaced by

$$|P_f^{\pi,(n)}| = \Delta t |f| a^{\pi,(n)} u^{\pi,(n)}. \tag{18}$$

It can be shown that this is a consistent approximation to the interface advection problem.

3.3 Momentum equations

3.3.1 Convection operator

The convection operator is very similar to that of [4]. This means that we use VoF fluxes to transport momentum, per phase, along with the interface. Our approach differs from that of [4] in a few ways:

- We use the dimensionally unsplit EMFPA scheme as the underlying advection scheme. This is mainly because dimensional splitting does not combine well with the fact that our divergence operator depends on the interface configuration via the face apertures (see Section 3.4.1).
- In [4] the liquid and gas momentum are 'merged' into a mass weighted velocity field $\bar{u}$ after each momentum transport step
$$\bar{u} = \frac{\{\!\{\rho\bar{\chi}u\}\!\}}{\{\!\{\rho\bar{\chi}\}\!\}}. \tag{19}$$
We skip this step since we allow the velocity field to be discontinuous.
- We use the Fromm scheme to compute the momentum fluxes.

3.3.2 Diffusion operator

We use a second order accurate diffusion operator (see eg. [11]) $\tilde{D}\tilde{G} : \mathcal{F}^h \to \mathcal{F}^h$ applied to $\bar{u}$ with a kinematic viscosity which is based on a weighted harmonically averaged dynamic viscosity

$$\bar{\nu} = \frac{\{\!\{\bar{\chi}^{(n)}\mu^{-1}\}\!\}^{-1}}{\{\!\{\rho\bar{\chi}^{(n)}\}\!\}} \leq \max\left(\frac{\mu^l}{\rho^l}, \frac{\mu^g}{\rho^g}\right). \tag{20}$$

The reason we use the mass weighted velocity field for diffusion is that we want our solution with a velocity discontinuity to converge to the ordinary Navier-Stokes solution (hence without velocity discontinuity) as soon as the interface boundary layer is resolved ($\Delta x \to 0$ or $\mathrm{Re} \to 1$).

3.3.3 Gravity

We model gravity according to the following finite volume discretisation

$$F^\pi = \rho^\pi a^\pi G(\mathbf{g} \cdot \mathbf{x}_i), \tag{21}$$

where $\mathbf{x}_i$ denotes the interface centroid, and reduces to the cell centroid $\mathbf{x}_c$ if the cell does not contain an interface. This model can be shown to sharply mimic the global conservation of energy as well as momentum.

3.3.4 Time integration

Since the convection operator does not follow the traditional method-of-lines approach, we must split the time integration. First we advect the momentum together with the interface (13)

$$|\omega^{\pi,*}|\rho^\pi u^{\pi,*} = |\omega^{\pi,(n)}|\rho^\pi u^{\pi,(n)} - \Delta t|\omega^{\pi,(n)}|\tilde{A}^\pi(u^{\pi,(n)})\left(\rho^\pi u^{\pi,(n)}\right), \tag{22}$$

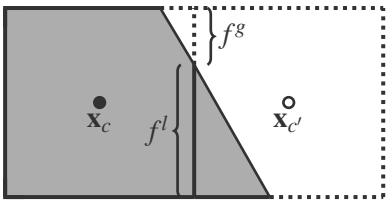

Figure 1: Illustration of the CCM. Each face is split into its liquid and gaseous part $f = f^l \cup f^g$. Shaded region corresponds to the liquid parts c^l, c'^l. Solid nodes correspond to the liquid phase and open nodes to the gas phase.

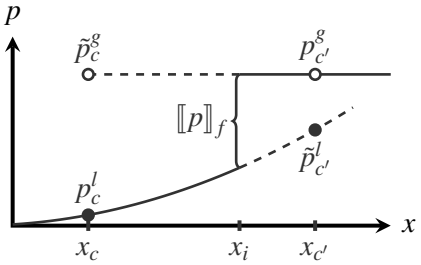

Figure 2: Illustration of the GFM. The pressure values denoted by $\tilde{p}$ are 'ghost' pressures and not actually part of the solution. Here $x_i = x_c + r_f^l(x_{c'} - x_c)$.

note that we write $|\omega^{\pi,*}|$ and not $|\omega^{\pi,(n+1)}|$, this is because the latter follows from the 'primary' volume fractions $\bar{\chi}^{(n+1)} \in \mathcal{C}^h$ according to (12), whereas the former follows from the staggered advection scheme. Then the diffusion operator and gravity force are applied

$$u^{\pi,**} = u^{\pi,*} + \Delta t \left[\bar{\nu} \tilde{D} \tilde{G} \bar{u}^* + \frac{1}{\rho^\pi \bar{\chi}^{\pi,(n+1)}} F^{\pi,(n+1)} \right]. \tag{23}$$

3.4 Pressure Poisson problem

Finally the divergence constraint (10) must be imposed, which is done via a pressure correction step

$$u^{\pi,(n+1)} = u^{\pi,**} - \Delta t g^\pi, \quad g^\pi(p) \approx \frac{1}{\rho^\pi} \eta_f \cdot (\nabla p^\pi)(\mathbf{x}_f), \tag{24}$$

for some pressure gradient g. We can now also impose the jump condition (7), since

$$\eta_{i_f} \cdot (Ju^{(n+1)})_f = 0 \quad \Rightarrow \quad \eta_{i_f} \cdot (Jg(p))_f = \Delta t^{-1} \eta_{i_f} \cdot (Ju^{**})_f, \tag{25}$$

where $(Ju)_f \approx [\![\mathbf{u}]\!](\mathbf{x}_f)$ and η_{i_f} is an approximate interface normal located at $\mathbf{x}_f$. Hence the pressure gradient $g^\pi(p)$ should incorporate two jump conditions at the interface: the Young-Laplace equation (8) as well as the newly introduced pressure gradient jump condition (25).

3.4.1 Divergence operator

The single fluid divergence operator $D : \mathcal{F}^h \to \mathcal{C}^h$ is given by

$$|c|(Du)_c = \sum_{f \in \mathcal{F}(c)} |f| \alpha_{c,f} u_f \approx \int_{\partial c} \mathbf{u} \cdot \eta \; dS. \tag{26}$$

At the interface two velocity fields exist, and the we therefore modify the divergence operator using the cut-cell method (CCM) [9].

$$|c|(D \{\!\{au\}\!\})_c \approx \int_{\partial c^l \setminus I} \mathbf{u}^l \cdot \eta \; dS + \int_{\partial c^g \setminus I} \mathbf{u}^g \cdot \eta \; dS \tag{27}$$

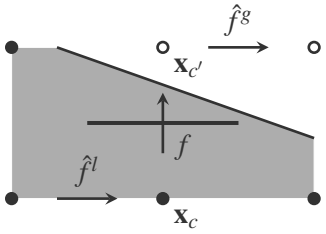

Figure 3: Example Md-GFM gradient stencil for an interface normal face $f \in \mathcal{F}_{I_\eta}$.

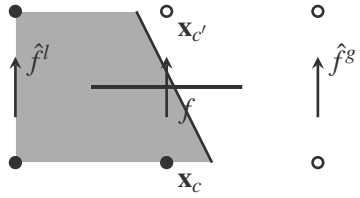

Figure 4: Example Md-GFM gradient stencil for an interface normal face $f \in \mathcal{F}_{I_\eta}$ where $\left|\frac{\alpha_{i_f,\hat{f}}}{\alpha_{i_f,f}}\right| > 2$.

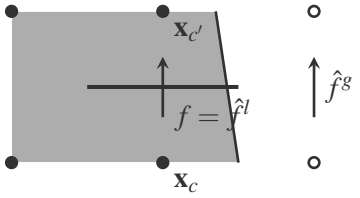

Figure 5: Example Md-GFM gradient stencil for an interface tangential face $f \in \mathcal{F}_{I_\tau}$.

where $|f| \{\!\{au\}\!\}_f = |f^l| u_f^l + |f^g| u_f^g$ is the total flux through the face f, see also Figure 1.

3.4.2 Gradient operator

In the interior of each of the fluid domains the gradient operator is simply the negative adjoint of the divergence operator

$$|\omega_f|(Gp)_f = -|\omega_f|(D^T p)_f = -|f| \sum_{f \in \mathcal{F}(c)} \alpha_{c,f} p_c \approx \eta_f \cdot (\nabla p)(\mathbf{x}_f). \tag{28}$$

At the interface we need to modify the gradient to take the two jump conditions into account. Here we use the ghost fluid method (GFM) [5], which results in

$$g^\pi(p) = \frac{1}{\{\!\{\rho r\}\!\}} \left[Gp + [\![p]\!] G\chi + [\![g(p)]\!] \hat{\rho}^\pi \right], \tag{29}$$

where $\chi_c = H_{\frac{1}{2}}(\bar{\chi}_c^l) \in \{0,1\}$ is the liquid indicator and $r^\pi \in [0,1]$ is the fraction of the line connecting $\mathbf{x}_c$ to $\mathbf{x}_{c'}$ which is covered in the π-phase, see also Figure 2. Moreover

$$\hat{\rho}^\pi = \begin{cases} -\rho^g r^g & \pi = l \\ \rho^l r^l & \pi = g \end{cases}, \tag{30}$$

such that $[\![\hat{r}]\!] = \{\!\{\rho r\}\!\}$ and $\{\!\{\rho r g\}\!\} = Gp + [\![p]\!] G\chi$. The latter equality shows that letting $r = \bar{\chi}$ results in momentum conservation if $[\![p]\!] = 0$.

3.4.3 The gradient jump

Note that $[\![g(p)]\!]_f \approx \eta_f \cdot \left[\!\left[\frac{1}{\rho} \nabla p \right]\!\right] (\mathbf{x}_f)$ which is not equal to $\eta_{i_f} \cdot \left[\!\left[\frac{1}{\rho} \nabla p \right]\!\right] (\mathbf{x}_f)$, unless the face normal η_f is aligned with the interface normal η_{i_f}. It follows that $[\![g(p)]\!]$ not known a priori, but rather depends on the pressure itself and therefore must be taken into account implicitly by generalizing the GFM to multi dimensional GFM (Md-GFM). We consider two different cases:

- An *interface normal face* is a face f between two cells $C(f) = \{c, c'\}$ whose centroids belong to a different phase (ie. $\chi_c \neq \chi_{c'}$). See also Figure 3. The set of all such faces is denoted by $\mathcal{F}_{I_\eta}$.
- An *interface tangential face* is a face f between two cells whose centroids belong to the same phase (ie. $\chi_c = \chi_{c'}$). See also Figure 5. The set of all such faces is denoted by $\mathcal{F}_{I_\tau}$.

We will describe each of the two cases for $d = 2$, the generalization to $d = 3$ is straightforward.

For an interface normal face f we select two neighbouring faces $\hat{f}^g, \hat{f}^l$ (whose neighbouring cells are gaseous and liquid respectively) whose face normal is orthogonal to that of f, see Figure 3. Using those faces we can define the jump interpolant J as follows

$$(Ju)_f = [\![u]\!]_f \eta_f + u_{\hat{f}^g} \eta_{\hat{f}^g} - u_{\hat{f}^l} \eta_{\hat{f}^l}, \tag{31}$$

which we can use to impose (25). This results in

$$[\![g(p)]\!]_f \alpha_{i_f,f} + g_{\hat{f}^g} \alpha_{i_f,\hat{f}^g} - g_{\hat{f}^l} \alpha_{i_f,\hat{f}^l} = \Delta t^{-1} \eta_{i_f} \cdot (Ju^{**})_f, \tag{32}$$

where $\alpha_{i_f,f} = \eta_{i_f} \cdot \eta_f$. From (32) we can solve the gradient jump $[\![g(p)]\!]_f$, which will depend on the surrounding pressure gradients. Solving for the gradient jump involves the ratio $\frac{\alpha_{i_f,\hat{f}}}{\alpha_{i_f,f}}$ (assuming wlog. that $\eta_{\hat{f}^g} = \eta_{\hat{f}^l}$), which can be arbitrarily large. We impose that the ratio can not exceed two in absolute sense, if the ratio does exceed two, we instead obtain the jump directly from neighbouring faces $[\![g(p)]\!]_f = \frac{1}{\rho^g}(Gp)_{\hat{f}^g} - \frac{1}{\rho^l}(Gp)_{\hat{f}^l}$, see Figure 4. This is always possible if the interface is resolved.

Now consider an interface tangential face f, which we assume to be in the liquid. Here we take a slightly different approach, we define the gradient as

$$g^l_f(p) = \frac{1}{\rho^l}(Gp)_f, \quad g^g_f(p) = \frac{1}{\rho^g}(Gp)_{\hat{f}^g}, \tag{33}$$

for a neighbouring gaseous face $\hat{f}^g$, see Figure 5.

The pressure Poisson problem can now be written as

$$\text{Find } p \in \mathcal{C}^h \text{ st. } D\{\!\{ag(p)\}\!\} = \Delta t^{-1} D\{\!\{au^{**}\}\!\}. \tag{34}$$

The linear part of the composed Laplace operator $L : p \mapsto D\{\!\{ag(p)\}\!\}$ can still be shown to be negative semi-definite, with only $p = 1$ in the nullspace. Movoerover due to the use of the CCM for the divergence operator, it is always guaranteed that the right-hand side is in the image of the Laplace operator, hence a unique (up to a constant) pressure exists.

4 RESULTS

4.1 Inviscid Kelvin-Helmholtz instability

In order to isolate the treatment of the velocity discontinuity we consider the simulation of an *inviscid* Kelvin-Helmholtz instability. We let the initial interface profile be given by

$$\eta(x,0) = \hat{\eta}(0)\cos(kx), \quad k = \frac{2\pi}{\lambda} = 1, \quad \hat{\eta}(0) = 5 \cdot 10^{-2}, \tag{35}$$

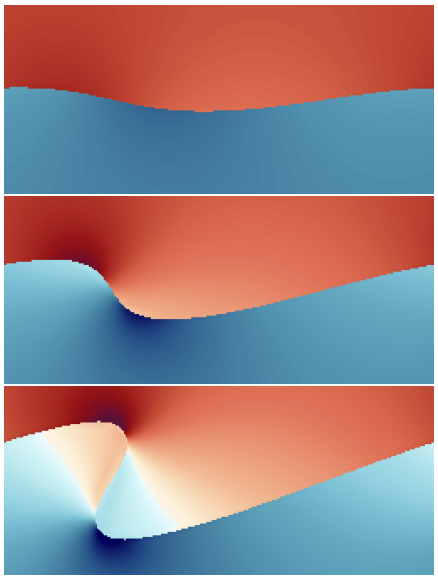

Figure 6: The x-component of velocity (clipped to the interval $[-1,1]$) at time instances $t/T = 0.8, 1.2$ and 1.6. Here $N_x = 2^8$.

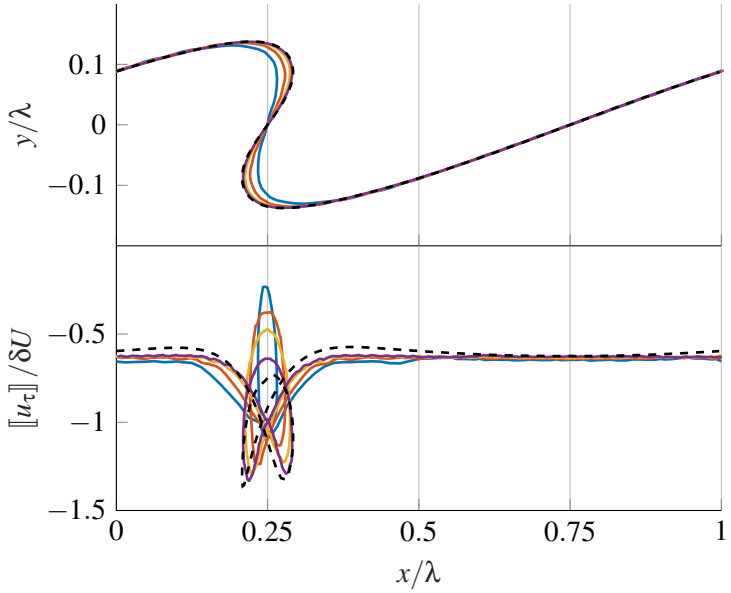

Figure 7: Convergence of the velocity discontinuity and interface profile at $t/T = 1.6$. The mesh is refined according to $N_x = 2^l$, where $l = 6,7,8,9$ (blue, red, yellow and purple). The dashed black line corresponds to the BI solution where $N = 2^9$.

where the domain is given by $\Omega = [0,\lambda] \times [-\lambda,\lambda]$ with slip boundary conditions applied to the top and bottom walls. The initial velocity field is given by $u^g = \delta U/2$, $u^l = -\delta U/2$ and the corresponding Weber number is given by

$$\mathrm{We} = \frac{\rho \delta U^2 \lambda}{\sigma} = 10\pi. \tag{36}$$

According to linear potential flow theory the interface will be unstable if $\mathrm{We} > 4\pi$ and moreover, out of the existing unstable modes which fit on our domain the one we initialized is expected to grow fastest.

In Figure 6 we show the evolution of the x-component of velocity where the time has been nondimensionalised using $T = \frac{\lambda}{\delta U}$. As a reference we use a boundary integral (BI) solution which has been obtained using the author's implementation of Method III described in [1]. Convergence to the reference solution can be observed in Figure 7.

4.2 Third-order Stokes wave

We consider the simulation of a third-order Stokes wave, for details about the initial conditions and domain size, see [2]. Contrary to [2] we do not initialize the velocity field in the gas phase. For a steepness of $\varepsilon = 0.55$ the initial condition results in a plunging breaker, see Figure 8. Here time has been nondimensionalised in terms of the wave period $T = \frac{2\pi}{\sqrt{gk}}$. The density ratio is given by $\rho^g/\rho^l \approx 1.17 \cdot 10^{-3}$. In the notation of [2], we let the Reynolds and Bond number be given by $\mathrm{Re} = 4 \cdot 10^4$ and $\mathrm{Bo} = 10^3$ resulting in 'easy to resolve' interface boundary layers and interface length scales. Hence this type of wave is appropriate for testing whether our model will converge to the desired Navier-Stokes

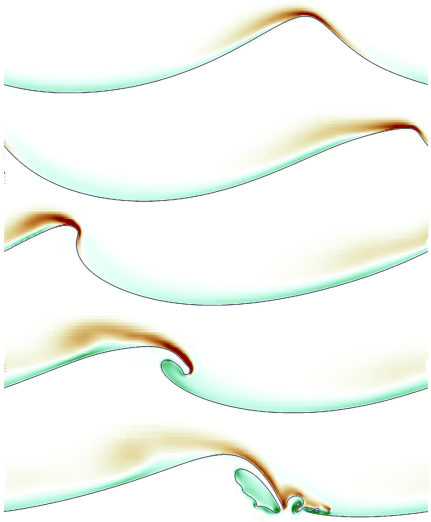

Figure 8: Vorticity (clipped to the interval $[-48,48]$) and interface profile on time instances $t/T = 0.16, 0.32, 0.48, 0.64$ and 0.8. Here $N_x = 2^9$ (using AMR).

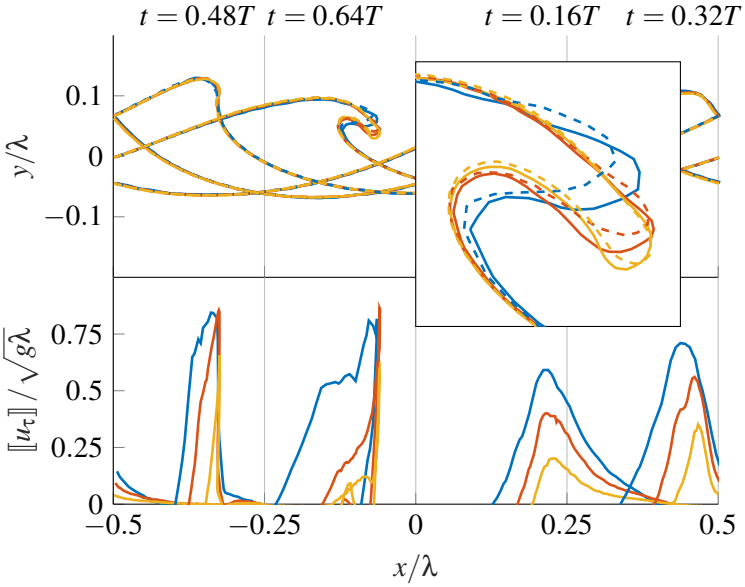

Figure 9: Convergence of the interface profile and tangential velocity discontinuity under mesh refinement for $N_x = 2^l$, where $l = 7, 8, 9$ (using AMR) corresponding to blue, red and yellow respectively. The dashed lines correspond to the single fluid model, whereas the solid lines correspond to our proposed two fluid model.

solution for a sufficiently fine mesh.

In Figure 9 we show the convergence of the interface profile at four time instances as well as the convergence of the tangential velocity jump $[\![u_\tau]\!]$ to zero. This shows that our two fluid model essentially reduces to a single fluid model once the interface boundary layers are resolved.

4.3 Large gas pocket impact

Finally we consider a high Reynolds number test case for which resolving the interface boundary layer is too expensive. We simulate a smooth dam break as found in [3], where the fluids (water and air) are initially at rest with the following interface profile

$$y = 7.6 + 3.6\tanh(0.44(x-15.5)), \tag{37}$$

on a domain given by $\Omega = [0,20]\times[0,12]\setminus e$, where e is an ellipse centered at $\mathbf{0}$ with radii given by 18 and 2.8 respectively.

Suppose we want $h < \lambda^{\mathrm{KH}}/4$ then we let $N_x = 80\cdot 2^l$, for $l = \lceil \log_2\left(\frac{1}{\lambda^{\mathrm{KH}}}\right)\rceil = 10$ based on $|[\![u_\tau]\!]| = 20$. Note that demanding $h < \lambda^{\mathrm{BL}}/4$ yields $l = 13$.

Make link between mesh resolution and introduction (that is, show solution with(out) slip when capillary length scales are resolved and estimate the BL thickness) and have a resolved simulation (!) up to t = 2.02?

5 DISCUSSION

Acknowledgements

This work is part of the research programme SLING, which is (partly) financed by the Netherlands Organisation for Scientific Research (NWO).

REFERENCES

[1] G. Baker and A. Nachbin. Stable methods for vortex sheet motion in the presence of surface tension. *SIAM Journal on Scientific Computing*, 19(5):1737–1766, 1998.

[2] L. Deike, S. Popinet, and K. Melville. Capillary effects on wave breaking. *Journal of Fluid Mechanics*, 769:541–569, 2015.

[3] S. Etienne, Y.-M. Scolan, and L. Brosset. Numerical Study of Density Ratio Influence on Global Wave Shapes Before Impact. In *ASME 2018 37th International Conference on Ocean, Offshore and Arctic Engineering.*, 2018.

[4] D. Fuster, T. Arrufat, M. Crialesi-Esposito, Y. Ling, L. Malan, S. Pal, R. Scardovelli, G. Tryggvason, and S. Zaleski. A momentum-conserving, consistent, Volume-of-Fluid method for incompressible flow on staggered grids. *arXiv preprint:1811.12327*, 2018.

[5] X.-d. Liu, R. P. Fedkiw, and M. Kang. A Boundary Condition Capturing Method for Poisson's Equation on Irregular Domains. *Journal of Computational Physics*, 160:151–178, 2000.

[6] J. Lopez, J. Hernandez, P. Gomez, and F. Faura. A volume of fluid method based on multidimensional advection and spline interface reconstruction. 195:718–742, 2004.

[7] J. E. Pilliod and E. G. Puckett. Second-order accurate volume-of-fluid algorithms for tracking material interfaces. *Journal of Computational Physics*, 199(2):465–502, 2004.

[8] S. Popinet. An accurate adaptive solver for surface-tension-driven interfacial flows. *Journal of Computational Physics*, 228(16):5838–5866, 2009.

[9] H. S. Udaykumar, H.-c. Kan, W. Shyy, and R. Tran-Son-Tay. Multiphase Dynamics in Arbitrary Geometries on Fixed Cartesian Grids. *Journal of Computational Physics*, 137(2):366–405, 1997.

[10] P. Van der Plas. *Local grid refinement for free-surface flow simulations*. PhD thesis, Rijksuniversiteit Groningen, 2017.

[11] R. Verstappen and A. E. P. Veldman. Symmetry-preserving discretization of turbulent flow. *Journal of Computational Physics*, 187(1):343–368, 2003.